DTU Library

Optimized method for multi-axial fatigue testing of wind turbine blades

Castro, Oscar; Belloni, Federico; Stolpe, Mathias; Yeniceli, Süleyman Cem; Berring, Peter; Branner, Kim

[Link back to DTU Orbit](#)

Journal Pre-proofs

Optimized method for multi-axial fatigue testing of wind turbine blades

Oscar Castro, Federico Belloni, Mathias Stolpe, Süleyman Cem Yeniceli, Peter Berring, Kim Branner

Please cite this article as: Castro, O., Belloni, F., Stolpe, M., Yeniceli, S.C., Berring, P., Branner, K., Optimized method for multi-axial fatigue testing of wind turbine blades, *Composite Structures* (2020), doi: https://doi.org/10.1016/j.compstruct.2020.113358

Optimized method for multi-axial fatigue testing of wind turbine blades

Oscar Castro[a,1,*], Federico Belloni[a,b], Mathias Stolpe[a], Süleyman Cem Yeniceli[a], Peter Berring[a], Kim Branner[a]

[a]*Technical University of Denmark, DTU Wind Energy, Frederiksborgvej 399, 4000 Roskilde*
[b]*Blade Test Centre A/S, Landdybet 10, 9220 Aalborg*

Abstract

An optimized method for testing wind turbine blades under fatigue is suggested. With this method, material-based damage targets along the blade are reached by applying an optimal combination of different uni- and multi-axial test blocks. The combination of test blocks is found using continuous linear optimization. Aeroelastic simulations are carried out to estimate both target and test strain-based damage in the blade. By applying the proposed method to a commercial wind turbine blade, the presented analysis illustrates that improved fatigue tests compared to current standard fatigue tests can be obtained in terms of both accuracy and total test time.

Keywords: Fatigue testing, Wind turbine blades, Optimization

1. Introduction

The time needed for the dynamic fatigue test of a large wind turbine blade can be several months. In Table 1, the expected fatigue test time as a function of blade length is shown. The natural frequencies for future long blades are estimated from engineering judgment based on those known for the DTU 10 MW reference wind turbine [1] with 86.4-meters blades. The test times take into account that tuning masses are added to match target loads and that tests

---

[*]Corresponding author
Email address: osar@dtu.dk (Oscar Castro)
[1]Telephone number: +45 93 51 13 33

regularly are stopped for inspections. It assumed that flapwise frequencies are reduced with 30% and edgewise frequencies with 15% due to tuning masses. It
10 is also assumed that 2 million cycles are applied in both flapwise and edgewise directions, and that total test time campaign (including inspections, etc.) is double that of the actual running test time. As can be seen, the test time for a 150-meters blade, for example, is expected to exceed one year when also instrumentation and static tests are included. Thus, there is a clear need to
15 shorten the test time.

Table 1: Expected fatigue test time as a function of blade length.

Blade length [m]	Natural frequency [Hz]		Test time [days]
	Flapwise	Edgewise	
86.4	0.61	0.93	167
100.0	0.50	0.75	205
120.0	0.41	0.61	251
150.0	0.32	0.47	323
200.0	0.23	0.33	453

Furthermore, these certification tests might not represent the real world very well [2]. In operations blades are exposed to torsion and bending in different directions at the same time. However, current standards [3, 4] describe to test the blades consecutively under flapwise and edgewise loading only. This
20 sequential approach to some extend omit the effects of combining the loads on the blade response. This may be a problem since the damage mechanisms that develop in composite materials and adhesive joints (the main components of wind turbine blades) under multi-axial fatigue loading can be different than the ones that develop under uni-axial loading conditions [5, 6]. Hence, the damage
25 mechanisms controlling the fatigue failure of wind turbine blades in operation might not be captured accurately in the test facilities and, therefore, not taken into account in the certification [7]. The wind-turbine-blade testing industry consequently also needs fatigue test methods that better match the loads to

2

which the blades are exposed to in real operational conditions. Considering all
this, this paper explores new possibilities to make fatigue tests for wind turbine
blades more realistic and efficient compared to current standard tests.

In order to make the fatigue tests more realistic, several methods to test
the blades in the flapwise and edgewise directions at the same time have been
proposed since the late 1990s. Hughes et al. [8], for example, were the first to
propose a bi-axial fatigue test by applying forced flapwise and edgewise excita-
tion through two ground-based exciters and a bell crank system. Even though
this method was a significant improvement compared to traditional single-axis
tests because better control of the load ratio and phase angle between the flap-
wise and edgewise loads were achieved, it was found that long test time and
very high energy consumption were needed to reach the target loads.

Based on these results, White [9] proposed to excite the blade at the reso-
nance frequency in order to decrease the test time and the energy consumption.
By using a flapwise resonance excitation combined with an edgewise forced ex-
citation, White showed that half the test time was saved with this method com-
pared to the method suggested by Hughes et al. Afterwards, other resonance
methods were also proposed. For example, resonance excitation was applied
in the edgewise direction while a forced excitation was applied in the flapwise
direction in [10, 11]. For this approach, no reduction of the test time was found
compared to the single-axis tests in addition to a greater difficulty level in con-
trolling the loads. Furthermore, methods in which the system is excited in res-
onance in both directions at the same time were proposed in [12, 13, 14, 15, 11].
For these methods, in contrast, it was found that an improvement of the test
time compared to single-axis tests and/or the level of accuracy respect to the
target loads can be obtained depending on the ratio between the flapwise and
edgewise loads.

The ratio between the flapwise and edgewise loads during bi-axial resonance
tests have been controlled mainly through two approaches. The first approach,
called *chaotic*, consists of controlling only the amplitude ratio between the two
load directions [12, 14, 16, 15, 17, 11]. By using this approach, faster fatigue

60 tests can be carried out compared to single-axis tests [15]. However, it has also been found that a significant overload can be generated in certain regions of the blade because the target loads in the flapwise and edgewise directions are not reached at the same time [16, 11]. Greaves [16], for example, found that the pressure side of the leading edge of a 100-meters blade was highly overloaded

65 when chaotic loads were applied, even though it was an improvement over single-axis tests. Nevertheless, Greaves et al. [17] managed to apply more realistic loads over a 40-meters blade while at the same time reducing the test time with 55% compared to single-axis tests. This was done by applying an optimal combination of chaotic load cases, which were defined by the number of cycles,

70 the pitch angle of the blades on the test stand and the amplitude ratio between the flapwise and edgewise loads.

In the second approach, called *phase-locked*, not only the amplitude ratio between the loads is controlled but also their frequency ratio and phase angle [18, 14, 16, 11]. By applying this approach, a better representation of the real

75 loading conditions can be obtained depending on phase angle and the frequency ratio between the loads. Greaves [16], for example, found that a phase angle of 66° provided the closest match between the test loads and the target loads at the root of a 100-meters wind turbine blade; whereas, Post [11] found a good match of the target loads of a 60-meters wind turbine blade when the frequency

80 ratio between the loads was 1:1. Moreover, the frequency ratio seems to affect also the test time. According to Post [11], a longer time than the single-axis tests was needed to complete the test of the evaluated 60-meters wind turbine blade when the frequency ratio between the flapwise and edgewise loads was 1:1. Whereas, for the same blade, around 40% improvement in the test time

85 compared to single-axis tests was reached when the flapwise-edgewise frequency ratio between the loads was 1:2.

A few papers have suggested optimization approaches to generate test setups that either maximize the accuracy level of the test loads respect to the target loads or minimize the total test time [19, 20]. Lee and Park [19], for example,

90 found an optimal flapwise test setup in which the exciter location was defined in

4

a way that the actuating force and the maximum error between the test loads and the target loads were minimized in a 48.3-meters blade. Whereas, Melcher et.al. [20] suggested an optimization scheme using virtual masses and spring elements to minimize the total test time, which can be applied to both uni-axial

95 and bi-axial test setups. By applying this method, they found that 30% of the total test time was saved in comparison with current standard tests.

As can be seen, all approaches have advantages and disadvantages in terms of testing time and level of accuracy with respect to target loads. However, most of them have not considered the cumulative effect of the applied loads based

100 on the corresponding strain or stress cycles, which ignores the actual effects of the loads on the material response. Moreover, little attention has been given to analyzing the contributions on the blade response and the test time when uni-axial and bi-axial load blocks are combined to reach material-level targets.

In this context, the present paper presents a new fatigue method for test-

105 ing wind turbine blades. The novelty of this method lies in finding an optimal combination of different uni- and multi-axial test blocks that allows reaching material-based targets along the blade both faster and more accurate than current standard test methods.

2. Methods

110 In this section, the suggested method for multi-axial fatigue testing of wind turbine blades is described. The section starts by describing the fatigue approach assumed to characterize the response of the blade under different test blocks. Then, the aeroelastic simulations needed to estimate such responses are explained. Finally, an optimization problem find the optimal combination of

115 test blocks is described.

2.1. Fatigue approach

In this approach, the effect of the applied loads on the fatigue response of the blade is accounted for at the material level, considering the longitudinal

strains along the span-wise blade direction, ε_z. These strains can be estimated
analytically using beam theories, such as the Euler-Bernoulli beam theory [21],
experimentally using, for example, strain gauges, or numerically using cross-
section analysis tools, such as BECAS [22] and VABS [23], or 3D finite element
models [24].

Following the fatigue approach suggested in [2], a point on the blade is
properly tested when the equivalent damage ratio, EDR_i, defined as the ratio
between the damage due to the test loads, D_i^{test}, and the damage expected
during operational conditions (i.e., the target damage), D_i^{tgt}, is equal or higher
than one, i.e. when

$$EDR_i = \frac{D_i^{test}}{D_i^{tgt}} = \left(\frac{\hat{\varepsilon}_{z,amp,i}^{test}}{\hat{\varepsilon}_{z,amp,i}^{tgt}}\right)^{\hat{m}} \geq 1 \tag{1}$$

where, $\hat{\varepsilon}_{z,amp,i}^{test}$ is the equivalent test strain amplitude, $\hat{\varepsilon}_{z,amp,i}^{tgt}$ is the equiva-
lent target strain amplitude, and $\hat{m}$ is the slope of the equivalent $\varepsilon - N$ curves,
see [2] for more details.

Note that D_i^{test} and D_i^{tgt} are independently estimated as follows [2]:

$$D_i = \frac{\hat{n}\hat{\varepsilon}_{z,amp,i}^{\hat{m}}}{\hat{b}} \tag{2}$$

where $\hat{n}$ is the equivalent number of cycles; $\hat{\varepsilon}_{z,amp,i}$ is chosen appropriately
as $\hat{\varepsilon}_{z,amp,i}^{test}$ or $\hat{\varepsilon}_{z,amp,i}^{tgt}$; and $\hat{b}$ is the inverse of $\log \hat{b}$, which is the intercept with
the $\log \varepsilon$-axis of the $\varepsilon - N$ curve for [2]the equivalent strain block [2].

Hence, the goal is to find a combination of test blocks that allows to properly
evaluate all the points in the blade by satisfying Eq. 1 and, at the same time,
minimizes the total test time and keeping EDR_i as close to one as possible.

It is worth to note that the fatigue approach suggested in [2] assumes a
linear cumulative damage model that follows the Palmgren-Miner's rule [25, 26].
Although the accuracy of this rule has been shown to be low for predicting the
fatigue life of composite materials under variable loading [27], this approach
is used in this study because the Palmgren-Miner's rule is currently the most
widely used damage accumulation model. More advanced cumulative damage

6

145   rules designed for composite materials, or damages based on the actual damage mechanisms developed in composite structures, could be used instead when they are available.

Before continuing with the description of the aeroelastic simulations, note as well that, in many cases, the information needed to estimate the strains in
150   the blades, such as airfoil geometry, material properties, material lay-up, or the cross-section properties, is not provided by blade manufacturers due to confidentiality reasons. In those cases, the modified bending moment, M'_β, proposed in [2] can be used instead. As shown in [2], this modified bending moment provides the same EDR_i than the strains, but only needs as inputs the bend-
155   ing moments applied to the structure and the ratio between the cross-sections stiffnesses, avoiding in this way compromise any confidential information about the blade design.

This method can be used, for example, to reproduce the results obtained in this study, see Section 3. Although in the present study EDR_i was estimated
160   based on strains, the calculation of EDR_i based on M'_β must produce the same results.

2.2. Aeroelastic simulations

The aeroelastic simulations needed to estimate the equivalent damage ratio (see Eq. 1) for different single- and multi-axial fatigue test blocks are described
165   in this section.

In order to estimate the equivalent test strain amplitude $\hat{\varepsilon}^{test}_{amp,ji}$ for the different fatigue test blocks j, aeroelastic simulations were carried out by means of a software for blade test simulations developed by DTU Wind Energy. In this software, the blade is modeled by using 3D Timoshenko beam elements
170   [28], oriented horizontally and constrained such that all six degrees of freedom at the root node are fixed. This mimics the test setup, where the blade is fully clamped to the test rig in a horizontal position by means of steel bolts.

The equation of motion used to model the blade response is defined as suggested in [16]. According to that, the structural damping matrix is obtained

7

175 using Rayleigh damping [16], and the gravitational force and the flapwise and edgewise aerodynamic forces are calculated according to [16].

The fatigue resonance testing is modeled by applying a resonance excitation to the blade at a specific longitudinal coordinate [16]. The excitation is defined as a mass translating on a straight path along the applied force direction at

180 a frequency equal to the blade first or second eigenfrequencies, depending on the test. Additionally, the so-called tuning masses used in these tests to adjust the dynamic blade response are modeled as concentrated masses and located at specific nodes.

The blade displacement is obtained using the Newmark-β time integration

185 method [29] and the internal element loads for each of the beam elements are found according to [16]. A simulation time t_0 is chosen which excludes the transient phase of the load application.

Strain time series for the chosen time period of t_0 are calculated at each analyzed blade location i using the applied loads and blade cross-sectional prop-

190 erties, as described in [2]. Based on these strain time series, and for each fatigue test block j, the equivalent test strain amplitude, $\hat{\varepsilon}_{amp,ji,t_0}^{test}$, is calculated.

According to this, different tuning mass distribution and excitation configurations were provided as input to the aeroelastic simulations in order to obtain the different test blocks. Single-axis flapwise and edgewise tests, bi-axial chaotic

195 tests and bi-axial phase-locked tests were simulated, as described in Section 3.1.

On the other hand, in order to estimate the equivalent target strain amplitude, $\hat{\varepsilon}_{amp,i}^{tgt}$, at the different blade locations i, aeroelastic simulations of the entire wind turbine were carried out similar to the aeroelastic simulations presented in [30]. The strain time series obtained from these simulations were

200 post-processed according to [2] in order to calculate the corresponding $\hat{\varepsilon}_{amp,i}^{tgt}$.

Once $\hat{\varepsilon}_{amp,ji,t_0}^{test}$ and $\hat{\varepsilon}_{amp,i}^{tgt}$ were obtained and based on Eq. 1, the equivalent damage ratio at the different blade locations i caused by the different test blocks

j for a given time period t_0, EDR_{ji,t_0}, were calculated as follows:

$$EDR_{ji,t_0} = \left(\frac{\hat{\varepsilon}_{amp,ji,t_0}^{test}}{\hat{\varepsilon}_{amp,i}^{tgt}} \right)^{\hat{m}} \qquad (3)$$

In the next section, an optimization method that combines the EDR_{ji,t_0}
205 from the different test blocks to minimize the total test time is proposed.

2.3. Optimization problem

An optimization problem for designing fatigue tests for rotor blades is proposed in this section. In this problem, a combination of test blocks j that minimizes the total test time, T, while keeping EDR_i at each point i of the blade
210 as close as possible to one, is found by solving a continuous linear optimization problem [31]. In this analysis, only the operational test time is considered. Changes in the test setup, stops for inspections and equipment maintenance, among others, are not included.

The optimization problem is modeled by introducing continuous variables
215 $x_j \geq 0$ describing the number of times that the test block j should be applied. The choice of modeling the variables as continuous rather than integer is motivated since the optimal variables, if non-zero, are expected to be large and that the errors and the total test time are only marginally influenced by rounding to the nearest integer.

Define the error e_i as the difference between the target equivalent damage ratio at each point i, $EDR_{i,tgt}$, which is assumed equal to one (meaning that D_i^{test} must be ideally equal to D^{tgt} at the end of the test, see Eq. 1) and the total equivalent damage ratio at the end of the test, $\sum_{j=1}^{n_l} x_j EDR_{ji,t_0}$, where n_l is the total number of evaluated test blocks. This is computed by the equality

$$e_i = EDR_{i,tgt} - \sum_{j=1}^{n_l} x_j EDR_{ji,t_0} \qquad (4)$$

which is linear in the variables x. The accumulated test time becomes a linear function of the variables through

$$T(x) = t_0 \sum_{j=1}^{n_l} x_j \qquad (5)$$

9

The optimization problem under consideration is then to minimize the total test time while satisfying limits on the errors, i.e. the problem

$$
\begin{aligned}
\underset{x \in \mathbb{R}^{n_l}}{\text{minimize}} \quad & T(x) \\
\text{subject to} \quad & \underline{e}_i \leq e_i(x) \leq \overline{e}_i \quad i = 1, \ldots, n_l \\
& x \geq 0
\end{aligned}
\tag{6}
$$

220   where $\underline{e}_i$ and $\overline{e}_i$ are user supplied lower and upper limits on the acceptable errors. Since the errors $e_i(x)$ are linear functions in the variables x, problem (6) is a linear optimization problem. Moreover, if the allowable errors are chosen to be too stringent the feasible set may very well be empty, i.e. there are not test blocks and/or time enough to come sufficiently close to the targeted values.

225   Since the problem is a linear optimization problem this situation can be robustly and correctly detected by modern numerical optimization methods and the user can be advised to increase the error bounds or to provide additional test blocks or test time.

The optimization problem can be efficiently and accurately solved by nu-

230   merical optimization methods based on either interior-point methods, see e.g. [32], or the Simplex method, see e.g. [31]. There exist many academic and commercial software implementing these methods and even if a large number of test blocks is suggested by the user, the corresponding optimization problems will be relatively modest scale (compared to other applications of linear

235   optimization) and one can expect to model and solve these problems within a matter of seconds.

3. Results

In order to show the capabilities of the proposed fatigue test method, a case study based on a commercial wind turbine blade is described in this section.

240   This blade is first analyzed according to the IEC 61400-23 standard [3] and then according to different optimization cases. The total test time and the equivalent damage ratio are compared between the different evaluated test cases. Finally, a more detailed description of the optimal solution is provided in order to better

10

explain the capabilities of the proposed method in finding an improved fatigue
test plan compared with the current standard test plan.

3.1. Case study

A commercial 14.3-meters wind turbine blade manufactured by Olsen Wings A/S [33] is used in this analysis in order to demonstrate the capabilities of the proposed method. All the information related to the blade structural properties is shown in Appendix A-Appendix C.

In this analysis, 18 cross-sections along the blade were analyzed, including the root, the transition region between the circular and the airfoil cross-sections, and the maximum chord, see Appendix B. In each of these cross-sections, 50 points (or stations) located at the external surface of the cross-sections were evaluated, see example in Fig. 1. The stations covered all cross-section regions, namely suction-side trailing-edge (SS-TE), suction-side spar-cap (SS-SC), suction-side leading-edge (SS-LE), pressure-side trailing-edge (PS-TE), pressure-side spar cap (PS-SC), and pressure-side leading-edge (PS-LE).

Figure 1: Example of stations evaluated within the blade cross-sections. Suction-side trailing-edge (SS-TE), suction-side spar-cap (SS-SC), suction-side leading-edge (SS-LE), pressure-side trailing-edge (PS-TE), pressure-side spar cap (PS-SC), pressure-side leading-edge (PS-LE).
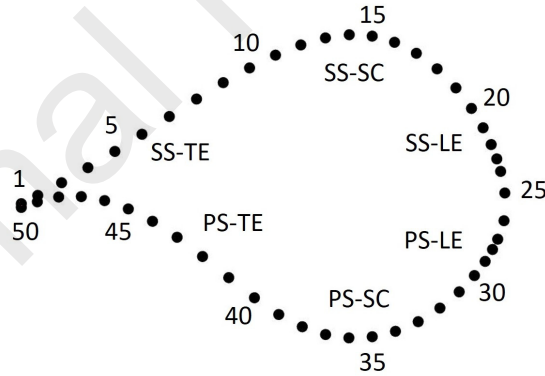
Several single edgewise and flapwise, and bi-axial chaotic and phase-locked test blocks were evaluated. The equivalent damage ratio EDR_{ji,t_0} caused by

each of these test blocks j at the different i stations for a given time period t_0, were calculated using Eq. 3. Aeroelastic simulations were carried out according to Section 2.2 in order to calculate $\hat{\varepsilon}_{amp,i}^{tgt}$ (see Appendix B and Fig. 2-a) and $\hat{\varepsilon}_{amp,ji,t_0}^{test}$. For that, $\hat{n}$ and $\hat{m}$ were assumed equal to 2E6 cycles and 10,
265 respectively. No mean correction of the strain amplitudes was done due to the lack of information regarding the material fatigue properties. Although this assumption affects the calculations on the actual effect of the loads on the material response, it does not compromise the purpose of this work on showing the advantages of the proposed method. In future analyzes, better estimates of
270 the material response can be carried out if manufactures provide information on the material properties.
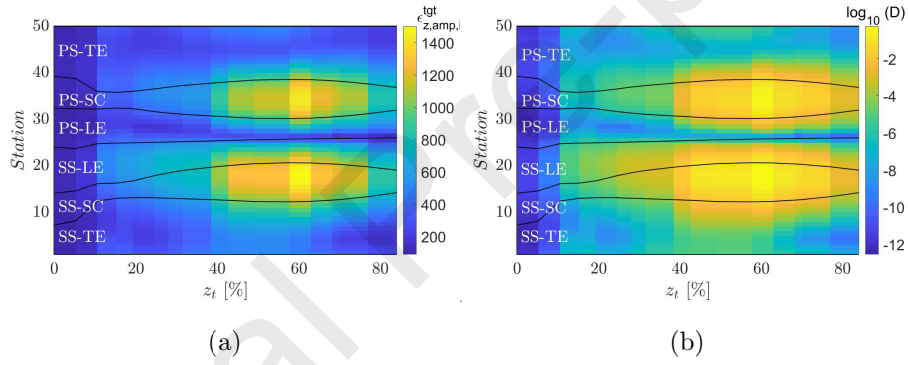
Figure 2: (a) Equivalent target strain amplitudes, $\hat{\varepsilon}_{amp}^{tgt}$, in micro-strains, and (b) damage target, D^{tgt}, along the blade for $\hat{m} = 10$ and $\hat{n} = 2E6$ cycles.

Furthermore, the blade structural damping was set to a value of 0.25% for the first and second eigenmodes, whereas the aerodynamic damping was modelled as described in Section 2.2. The drag coefficient was assumed equal to 2.7 for
275 all blade cross-sections [34, 35]. The $\hat{\varepsilon}_{amp,ji,t_0}^{test}$ strains were calculated for the different test blocks j, which were defined by varying both the values of the tuning masses along the blade and the exciter configuration in both flapwise and edgewise directions, see Table 2.

As shown in Table 2, four tuning mass locations, z_t, were defined at 21.0%,

12

Table 2: Tuning mass, m_t/m_{blade}, blade excitation, F/EC, and phase angle, ϕ, input data at pre-defined span blade locations, z_t, needed to define different test setups to be evaluated during the optimization.

	m_t/m_{blade}			F/EC			
z_t [%]	min	increment	max	type	min	increment	max
21.0	0.43	0.13	1.00	edgewise	0.0	0.03	0.46
31.5	0.53	0.13	1.00	flapwise	0.0	0.17	0.86
42.7	0.00	0.05	0.40	-	-	-	-
69.9	0.00	0.03	0.13	-	-	-	-
Phase angle, ϕ [°] (only for phase-locked cases)							
min			increment			max	
15			15			165	

31.5%, 42.7%, and 69.9% of the blade span. For each of these locations, six possible tuning masses, m_t, were considered, which were established based on predefined minimum and maximum mass values, and a certain mass increment. Consequently, 1620 tuning mass distributions were analyzed, which were obtained as a result of combining the different tuning mass values at different locations. The tuning mass values were normalized with respect to the blade mass, i.e., $m_{blade} = 750kg$.

Moreover, for each of these tuning mass distributions, different exciter configurations were analyzed, see Table 2. The locations of the edgewise and flapwise exciters were defined at 21.0% and 31.5% of the blade span, respectively. Different exciter load levels, F, were considered in the two directions, which varied from zero to a maximum value, every certain load increment. In this way, the edgewise, flapwise, and chaotic test block configurations were defined. The exciter load levels were normalized with respect to the load capacity of the exciters, EC, in the corresponding direction, i.e., $EC_{edge} = 3.5kN$ and $EC_{flap} = 7.0kN$.

Phase-locked 1:2 test block configurations were also included. This type of phase-locked case was chosen because it is closer to the intrinsic flapwise-edgewise-natural-frequency ratio of the blade. No phase-locked 1:3 test block

13

configurations were analyzed because they would require in reality the use of 1D masses [11] to decrease the edgewise natural frequency to the desired level.

300 This would make the test setup complex and difficult to implement, especially for large wind turbine blades. In this sense, only the previously-defined test block configurations that had a frequency ratio of 0.5 ± 0.0001 were considered to define the phase-locked cases. For these cases, phase angles, ϕ, from $15°$ to $165°$ every $15°$ were taken into account, see Table 2.

305 For the test equivalent strains, $\hat{\varepsilon}_{amp,ji,t_0}^{test}$, a simulation time $t_0 = 100s$ was used, which excluded the transient phase of the load application. The simulation time was chosen by using the least common multiple value [36], as described in [16]. This simulation time was found sufficient as the applied load frequencies in the flapwise direction, f_{flap}, for all evaluated biaxial cases were within a range of 310 1.829 Hz - 2.240 Hz, and the applied load frequencies in the edgewise direction, f_{edge}, for all evaluated biaxial cases were within a range of 3.714 Hz - 4.667 Hz. Moreover, the f_{flap} and f_{edge} frequencies were normalized respect to the natural frequencies of the blade in the corresponding directions, $f_{blade,flap} = 2.286 Hz$ and $f_{blade,edge} = 4.762 Hz$.

315 In all cases, the maximum and minimum test loads that excited the limits imposed by the blade ultimate loads (see Fig. Appendix C) were not considered within the optimization. Not considering these test cases might be conservative as blades could survive higher loads than the ultimate ones, as shown in [37]. However, as this behavior might change from blade to blade and no previous 320 information in this regards was known for the blade under consideration, it was decided to be conservative. Nevertheless, it is worth noting that including the test cases with higher loads within the optimization might improve the results obtained from the proposed method as shorter test times could be achieved.

The optimized solutions were obtained by solving the linear program outlined 325 in Section 2.3. In all cases, the lower error limit, $\underline{e}_i$, was set equal to 0 to ensure that all the points reach the targets. The upper error limit, $\overline{e}_i$, was assumed equal to infinity to allow the algorithm to find the shortest total test time.

Different fatigue test solutions were analyzed, including the standard test

14

solution and different optimized solutions. The different optimized solutions
330 covered the cases in which each type of loading condition (i.e., uniaxial, chaotic,
and phase-locked 1:2) was analyzed independently and when all of them were
combined. The different optimized solutions were compared with the standard
test in terms of total test time, $T/Tstd$, minimum and maximum equivalent
damage ratio, EDR_{min} and EDR_{max} respectively, and maximum fatigue test
335 damage, D_{max}^{test}.

The fatigue test damage, D^{test}, was estimated based on Eq. 2 and it was
used just as a benchmark point in terms of possible fatigue failures of the blade
under the different obtained fatigue test solutions. According to Eq. 2, a value
of $\hat{b} = 0.0068$ was assumed, which corresponds to the static strain strength in
340 compression of a typical glass/epoxy material [1], including a safety factor of
2.205 according to [38]. A limit damage fraction equal to the unity (i.e., $D_i = 1$)
was also assumed as a reference in this study, although it has been shown that
the failure in composite materials can happen for smaller or larger limit damage
fractions than one (i.e., $D_i \neq 1$) [27].

345 Similarly, the total damage corresponding to the equivalent target strain
amplitude, D^{tgt}, was also estimated assuming $\hat{b} = 0.0068$, see Fig. 2-b. As
shown in this figure, the blade seems not to fail after the operational lifetime is
reached.

In the following sections, the results related to the total test time and the
350 fatigue response of the blade for the standard fatigue test and the different
optimized fatigue tests are presented.

3.2. Standard test

In current standard fatigue tests, the blades are usually tested consecutively
under flap-wise and edgewise fatigue loading, considering only target fatigue
355 bending moments, M^{tgt}, in these two directions [3, 4]. For that, tuning masses
are located along the blade and loads are applied in a way that the target
bending moments are reached by the test fatigue bending moments, M^{test}, in
the most critical regions of the blade after the equivalent number of cycles $\hat{n}$ is

15

applied.

360   Accordingly, the normalized tuning mass distributions, m_t/m_{blade}, the normalized excitation configurations, F_{flap}/EC_{flap} and F_{edge}/EC_{edge}, and the normalized frequencies with which the loads were applied to the blade, $f_{flap}/f_{blade,flap}$ and $f_{edge}/f_{blade,edge}$, defined to carry out the standard flapwise and edgewise fatigue test simulations for the blade under study are shown in Table 3. See

365   values of m_{blade}, EC_{flap}, EC_{edge}, $f_{blade,flap}$, and $f_{blade,edge}$ in Section 3.1. Additionally, the time needed to carry out each test block, t_{block}, is also shown in Table 3, which was normalized respect to the total test time, T_{std}.

These test setups were defined to reach the M^{tgt} moments in the two directions (see Appendix C) in most of the regions between the root and 70%

370   of the blade span (see, Fig. D.11), according to suggestions provided by the manufacturer. The minimum and maximum test fatigue bending moments did not exceed static ultimate moments, as shown in D.12.

Table 3: Test scenarios for the standard test.

Tuning masses		Blade excitation			
Single-axial flapwise ($t_{blk,flap}/T_{std} = 65.4\%$)					
z_t [%]	m_t/m_{blade}	F_{flap}/EC_{flap}	F_{edge}/EC_{edge}	$f_{flap}/f_{blade,flap}$	$f_{edge}/f_{blade,edge}$
21.0	0.43	-	-	-	-
31.5	0.53	0.86	-	0.98	-
42.7	0.18	-	-	-	-
Single-axial edgewise ($t_{blk,edge}/T_{std} = 34.6\%$)					
z_t [%]	m_t/m_{blade}	F_{flap}/EC_{flap}	F_{edge}/EC_{edge}	$f_{flap}/f_{blade,flap}$	$f_{edge}/f_{blade,edge}$
21.0	0.97	-	0.20	-	0.89
31.5	0.67	-	-	-	-
42.7	0.13	-	-	-	-
69.9	0.05	-	-	-	-

The EDR_i ratio along the blade after the simulated standard fatigue test is shown in Fig. 3. As shown in Fig. 3-a, many regions along the blade over-pass

16

375 the target strain-based damage, $EDR_{i,tgt}$, of one assumed in Section 2.3. The the regions with higher EDR_i are the ones at the spar caps close to the root and at the SS-LE and PS-TE regions towards the caps at around 65% of the blade length. The EDR_i ratio after each block test is shown in Fig. D.13.
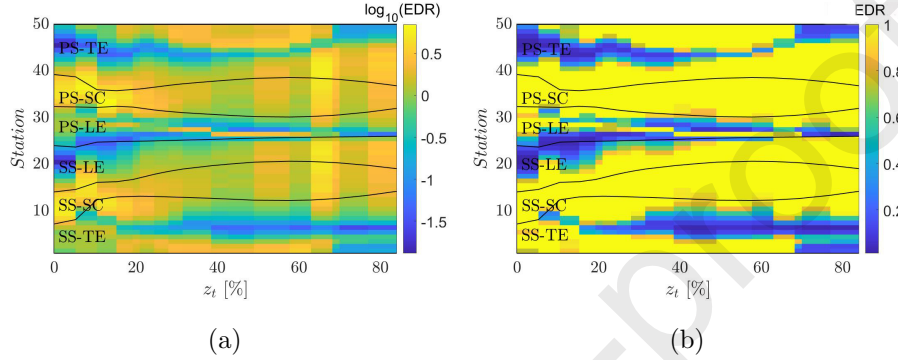
Figure 3: EDR after the simulated standard fatigue test with a colorbar scale up (a) to the maximum value, in log scale, and (b) to one. The yellow regions on the right-side plot correspond to the ones that are on or above of target.

Furthermore, in Fig. 3-b, the regions in which the $EDR_{i,tgt}$ ratio is reached
380 (or over-passed) are shown in yellow, while the regions under target are shown in other different colors. As seen in Fig. 3-b, the spar-caps are on target all along the blade span; whereas, the trailing-edge and leading-edge are on target from %5 to %65 of the blade span. Nevertheless, the regions in between the spar-caps and the trailing-edge and leading-edge along on the entire blade, in
385 which the sandwich panels are normally located, do not reach the strain-based target damage.

Even though some regions over-passed the $EDR_{i,tgt}$ ratio, the blade seems not to fail after the test is completed, see Fig. 4. As shown in Fig. 4, the higher test damage is located at the spar-caps in a region between 40% and 80% of the
390 blade span.

Based on all this, the question is now: Can the strain-based target damage be reached in the entire blade both faster and more accurately compared to the standard tests? This question will be answered in the next sections.

17
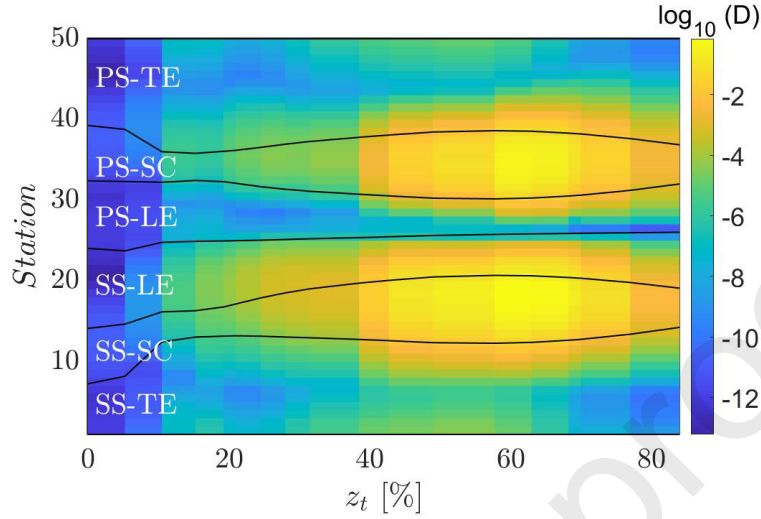
Figure 4: Total damage, D^{test}, along the blade after the standard fatigue test. In log scale.

3.3. Comparison between standard test and optimized solutions

In this section, the different optimized fatigue test solutions are analyzed. As shown in Table 4, and contrary to the standard test, all optimized solutions reach the strain-based target damage in all the blade stations as EDR_{min} is equal to the unity in all of them. Nevertheless, EDR_{max} is significantly higher for the optimized solutions than for the standard test. Moreover, in the optimized cases in which only uniaxial loads or phase-locked loads are considered, D_{max}^{test} is higher than the unity; whereas, in the cases in which only chaotic loads are considered, or all types of loads are combined, the blade does not seem to fail as D_{max}^{test} is lower than one. In fact, the D_{max}^{test} damage for the last two cases is slightly lower than the one obtained from the standard test.

Furthermore, a longer test time is necessary when considering only optimized uniaxial or phase-locked tests than for the standard test, see Table 4. Conversely, around 50% reduction in total test time compared to the standard test time can be obtained when only chaotic loads are considered or all types of loads are combined. This means that, for the last two optimized cases, not only more accurate but also faster tests are obtained.

18

Table 4: Comparison between the standard test and different optimized solutions.

	$T/Tstd$	EDR_{min}	EDR_{max}	D_{max}^{test}
Standard (no optimized)	1.00	0.02	6.96	0.70
Uniaxial	6.66	1.00	839.96	26.02
Chaotic	0.53	1.00	187.22	0.65
Phase-locked 1 : 2	2.84	1.00	414.47	2.28
All combined	0.50	1.00	170.78	0.69

Additionally, it was found that in the case of only chaotic cases are considered, five different chaotic configurations are needed to obtain the optimal solution; whereas, in the case in which all test blocks are combined, four chaotic configurations and one single-axial edgewise configuration are needed for the same purpose. This indicates that, for the evaluated blade, chaotic loads can provide better solutions than the independent single-axial loads applied in the standard test, but an even better solution can be found when the chaotic loads are complemented with single-axial cases.

In the next section, a more detailed description of the results obtained from the all-combined-loading optimal solution is presented.

3.4. All-combined-loading optimal solution

The normalized tuning mass distributions, m_t/m_{blade}, the normalized excitation configurations, F_{flap}/EC_{flap} and F_{edge}/EC_{edge}, and the normalized frequencies with which the loads were applied to the blade, $f_{flap}/f_{blade,flap}$ and $f_{edge}/f_{blade,edge}$, for the all-combined-loading optimal solution are shown in Table 5. See values of m_{blade}, EC_{flap}, EC_{edge}, $f_{blade,flap}$, and $f_{blade,edge}$ in Section 3.1.

As shown in Table 5, four chaotic cases and one single-axial edgewise case applied during different time periods, t_{blk}/T, define this optimal solution. In the case of the chaotic scenarios, different tuning mass distributions and different load configurations are needed. Note that no phase-locked case is included in the solution. The minimum and maximum test fatigue bending moments in the

19

different configurations within this optimal solution did not exceed the static ultimate moments, see Fig. E.14.

435   With this optimal solution, the EDR_i ratio is reached all over along the blade, see Fig. 5-b. The regions with the higher EDR_i are the ones at the root between PS-SC and PS-LE, and between SS-SC and SS-TE, see. Fig. 5-a. Whereas, the regions with the lower EDR_i are at the root at PS-TE and SS-LE far from the spar-caps, and in the spar-caps towards the tip from 40% the blade

440   span. The equivalent damage ratio, EDR_i, after each block test within the optimal solution is shown in Fig. E.15.
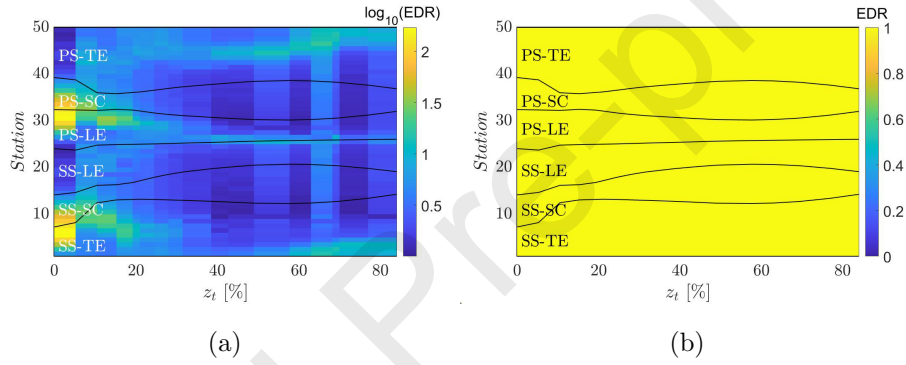
Figure 5: EDR after the all-combined-loading optimized fatigue test with a colorbar scale up (a) to the maximum value, in log scale, and (b) to one. The yellow regions on the right-side plot correspond to the ones that are on or above the target.

    Furthermore, a comparison between the EDR_i ratio in the different cross-section regions along the blade for the standard test and the all-combined-loading test is presented in Fig. 6. As shown in this figure, and as described

445 before, the EDR_i ratio is reached everywhere in the blade when the optimal solution is considered. Whereas, for the standard fatigue test, many areas within the cross-section regions are not well tested, especially the ones where the sandwich panels are normally located. In addition, for the optimal solution, the EDR_{max} at each cross-section is higher close to the root, but start decreas-

450 ing towards the tip. In fact, EDR_i tends to one in almost all stations in the

20

Table 5: Test scenarios for the all-combined-loading optimal solution.

Tuning masses		Blade excitation			
Chaotic No 1 ($t_{blk}/T = 1.9\%$)					
z_t [%]	m_t/m_{blade}	F_{flap}/EC_{flap}	F_{edge}/EC_{edge}	$f_{flap}/f_{blade,flap}$	$f_{edge}/f_{blade,edge}$
21.0	0.83	-	0.17	-	0.79
31.5	1.00	0.86	-	0.81	-
42.7	0.07	-	-	-	-
69.9	0.13	-	-	-	-
Chaotic No 2 ($t_{blk}/T = 81.3\%$)					
z_t [%]	m_t/m_{blade}	F_{flap}/EC_{flap}	F_{edge}/EC_{edge}	$f_{flap}/f_{blade,flap}$	$f_{edge}/f_{blade,edge}$
21.0	0.83	-	0.20	-	0.94
31.5	1.00	0.86	-	0.97	-
42.7	0.18	-	-	-	-
Chaotic No 3 ($t_{blk}/T = 0.9\%$)					
z_t [%]	m_t/m_{blade}	F_{flap}/EC_{flap}	F_{edge}/EC_{edge}	$f_{flap}/f_{blade,flap}$	$f_{edge}/f_{blade,edge}$
21.0	0.97	-	0.20	-	0.79
31.5	0.93	0.86	-	0.82	-
42.7	0.18	-	-	-	-
69.9	0.13	-	-	-	-
Chaotic No 4 ($t_{blk}/T = 1.8\%$)					
z_t [%]	m_t/m_{blade}	F_{flap}/EC_{flap}	F_{edge}/EC_{edge}	$f_{flap}/f_{blade,flap}$	$f_{edge}/f_{blade,edge}$
21.0	1.00	-	0.20	-	0.91
31.5	0.53	0.86	-	0.92	-
69.9	0.05	-	-	-	-
Single-axial edgewise ($t_{blk}/T = 14.0\%$)					
z_t [%]	m_t/m_{blade}	F_{flap}/EC_{flap}	F_{edge}/EC_{edge}	$f_{flap}/f_{blade,flap}$	$f_{edge}/f_{blade,edge}$
21.0	0.70	-	0.23	-	0.98
31.5	0.93	-	-	-	-

cross-sections close to the tip.
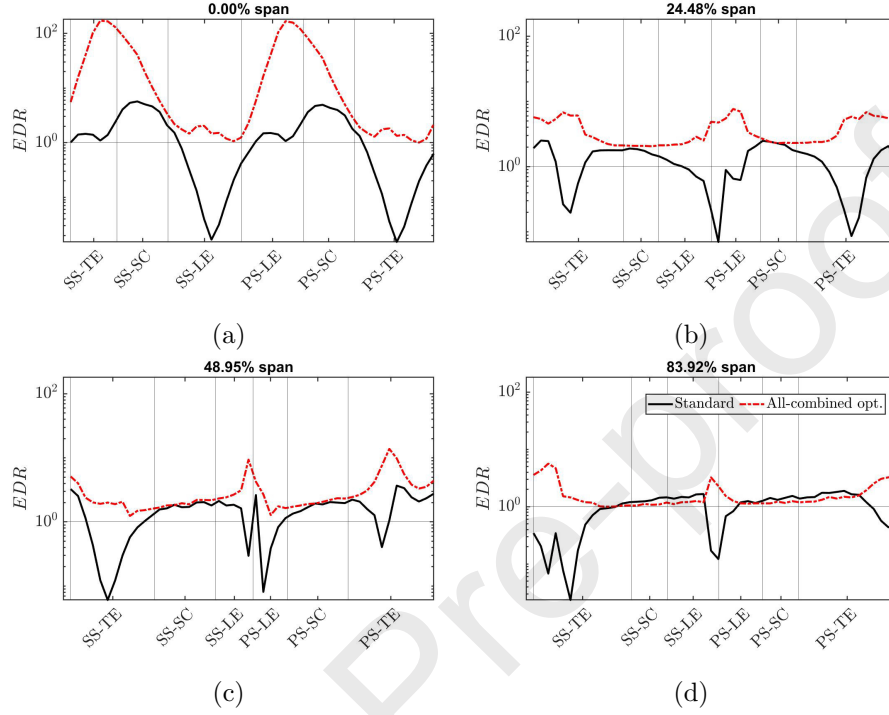
Figure 6: Comparison between the EDR for the standard test and the all-combined-loading optimized fatigue test at different blade spans: (a) 0.00%; (b) 24.48%; (c) 48.95%; and (d) 83.92%.

Although some regions exceeded the $EDR_{i,tgt}$ ratio, especially the ones close to the root (see Fig. 5-a), the blade seems not to fail as D_{max}^{test} is lower than one, see Fig. 7. As shown in this figure, the higher damage is located at the spar-caps in a region between 40% and 80% of the blade span. This region and the damage level are similar to the ones obtained from the standard fatigue test, see Fig. 4.

4. Discussion

In the previous section, it was shown that faster and more accurate fatigue tests than the ones suggested by current standards can be obtained for the

22
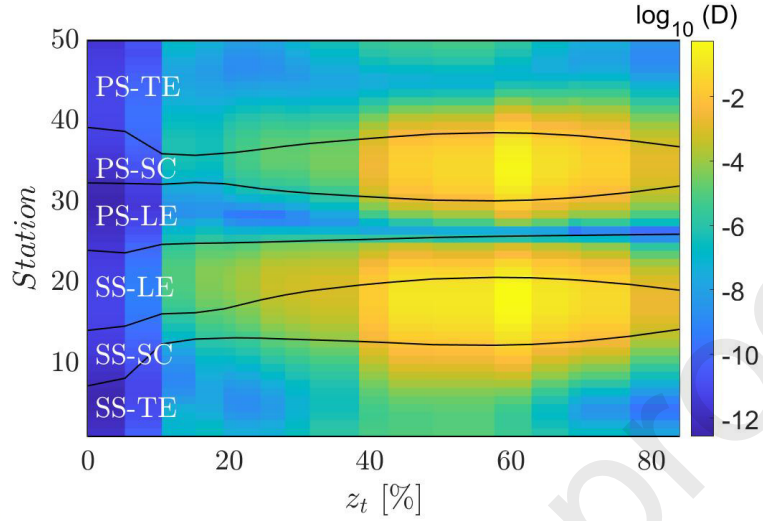
Figure 7: Total damage, D^{test}, along the blade after the all-combined-loading optimized fatigue test. In log scale.

blade under study by implementing the suggested optimization testing method. In this section, an explanation of how this may be possible, the benefits of these improvements and possible future ways to find even better solutions are discussed.

465   When bending moments in the flapwise and edgewise directions are applied independently during the test, only the cross-section regions located in these two directions (e.g., spar-caps, leading-edge, and trailing-edge) can reach the strain-based target damage once the equivalent-fatigue-bending-moment targets are reached [2]. This means that longer tests would be needed to achieve the strain-470 based target damage in other regions, such as sandwich panels, causing at the same time over-testing and possible failures in the spar-caps, leading-edge, and trailing-edge.

     This explains why, for the standard test case, the EDR ratio is equal or higher than one only at the spar-caps from the root to %80 of the blade span, 475 and at the trailing-edge and leading-edge from %5 to %65 of the blade span (see Fig. 3-b), since the target flapwise and edgewise bending moments are reached

23

in these regions respectively, see Fig. D.11. This also explains why, for the optimized solution considering only uniaxial test blocks, a test time 6.6 times longer than the one for the standard test is needed to reach the strain-based

480 damage everywhere in the blade, and possible failure can happen as D_{max}^{test} is significantly higher than the unity, see Table 4.

On the other hand, when multi-axial loads are applied instead, not only the cross-section regions at the flapwise and edgewise directions can reach the strain-based target damage, but also the others, as shown in Sections 3.3 and 3.4. This

485 is because the direction of the resultant bending moment is different than the flapwise and edgewise directions and changes as the magnitude, frequency, and phase angle of the flapwise and edgewise bending moments change. This can help to better test the different cross-section regions and to decrease the total test time as the loads are applied simultaneously, as explained in [15].

490 This can be seen, for example, when only chaotic test blocks were considered in the optimization process, see Table 4. As shown in this table, the strain-based target damage was reached in all points much faster and with less damage than the optimized solution considering only uniaxial test blocks. This is because, when a chaotic load is applied during a certain time (see Fig. 8), several loading

495 patterns are obtained as the phase angle is not controlled and, therefore, several cross-section points can be excited at the same time. Moreover, the reduction of time obtained in this solution agrees with what was found by Greaves et al. [17], in which 55% of the test time was safe in comparison with standard tests when an optimal combination of chaotic load cases was applied to a 40-meters

500 blade.

However, longer and more damaging tests were obtained when only phase-locked were considered in the optimization process compared to the standard solution. This is because, for the phase-locked cases, specific cross-section points are excited depending on the magnitude and frequency of the flapwise and edge-

505 wise bending moments, but especially on the phase angle between these two moments [11]. As shown in Fig. 9, for a specific load level and frequency ratio, different load patterns can be obtained for different phase angles, which

24
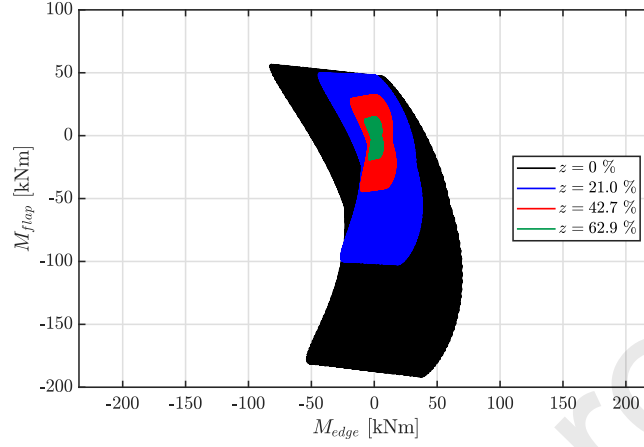
Figure 8: Example of bi-axial chaotic test case: bending moment envelope along the blade.

affect only specific cross-section points. This means that several phase-locked cases and longer test time are needed to reach the targets in the entire blade, which could also cause an over-testing in some of the cross-section regions and, therefore, possible failures, as shown in Table 4.

(a)   (b)
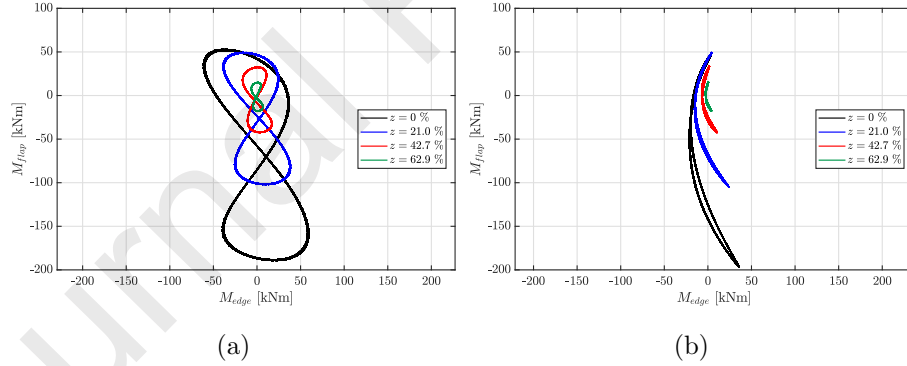
Figure 9: Example of bi-axial phase-locked 1:2 test case: bending moment envelope along the blade surface for (a) $\phi = 10°$, and (b) $\phi = 40°$.

These results contradict in some way what was found by Post, [11], in which around 40% improvement in the test time compared to standard tests was reached when phase-locked 1:2 loading were applied to a 60-meters wind turbine blade. In that case, the the natural frequency ratio of the blade was also

25

closer to 1:2. The possible difference between the two studies is that, in [11], the target damage was accounted for in terms of fatigue bending moments and not on strains. In that study, the equivalent number of cycles, $\hat{n}$, is equal to 1E6 and 2E6 cycles for the flapwise and edgewise directions, respectively; which was

520   used as reference not only to complete the standard tests but also to complete the phase-locked test. This makes the time needed to complete the phase-locked test lower than the one needed to reach target strain-based damage based on $\hat{n} = 2E6$ cycles, as the one assumed in the present study.

In spite of this, it is worth to say that the phase-locked cases could be
525   beneficial when specific regions within the cross-sections are to be tested, for example, when damages located at specific locations in the blade are to be evaluated.

Nevertheless, the main advantage of the optimization method proposed in this work is that it considers the benefits of using different uni- and multi-
530   axial test configurations to reach target damages at the material level. For example, for the blade evaluated in this study, different chaotic test blocks were complemented by a single-axial edgewise test block to make the test even faster and more accurate, see Sections 3.3 and 3.4. In this case, the different chaotic configurations contribute to quickly reach the target strain-based damage in
535   most of the cross-section stations, see Fig. 10; whereas, the single-axial edgewise configuration contributes to exciting only a few stations at the leading-edge and trailing-edge in order to reach the target in these areas. In this way, it was avoided to significantly over-testing the regions that already reached the damage targets (see Fig. 10) and, at the same time, decreasing the testing time.

540   In fact, even faster and more accurate solutions can be obtained with the proposed optimization method if the input data to optimize is improved. One way to do this is by not considering in the optimization process the regions of the blade that are not critical. Another way is by better defining the test configurations to be optimized. In particular, by considering tuning mass dis-
545   tributions and loading configurations that can ensure that different percentages of the blade span can be tested without considerably affecting the rest of the

26
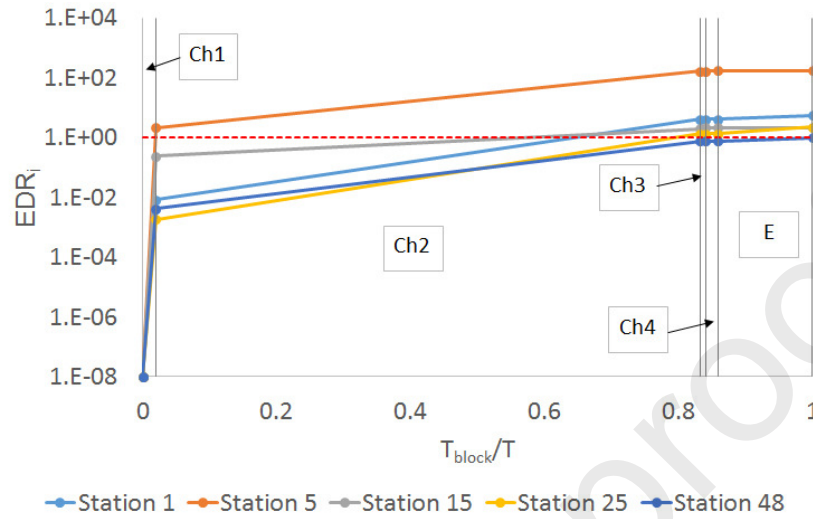
Figure 10: Damage contribution of the different block tests within the optimal solution (i.e., chaotic 1, Ch1; chaotic 2, Ch2; chaotic 3, Ch3; chaotic 4, Ch4; and single-axial edgewise, E) to the blade stations. The stations at the root are shown as an example. See Fig. 1 for the station enumeration within the cross-section.

blade. By doing this, for example, the over-testing at the root shown in Fig. 6-a could have been reduced. Note that the more test configurations to evaluate, the greater the need for computational resources to run the simulations, espe-
550 cially the aeroelastic ones. Hence, we must find a way to minimize the number of possible cases to evaluate, but that in turn, they contribute more to the final solution.

5. Conclusions

An optimized method for multi-axial fatigue testing of wind turbine blades is
555 proposed. By applying the proposed method, improved fatigue tests compared to current standard fatigue tests are obtained in terms of both accuracy and total test time. This is achieved by considering several possible test configurations, minimizing the total test time, and satisfying predefined error limits. Moreover, the response of the blade is accounted for at the material level by considering
560 strain-based damage targets.

27

The proposed optimization method was applied to a commercial wind turbine blade in order to illustrate its capabilities. Contrary to standard tests, it was found that all regions along this blade reached the strain-based target damage when using the proposed optimization method, along with the fact that no failure due to static and fatigue loading was predicted. This was done by combining four different chaotic cases with a single-axial edgewise case. In addition, it was found that the equivalent damage ratio, EDR, in most of the blade stations tended to one. This indicated that the over-testing was significantly reduced in most of the blade. Furthermore, a reduction of 50% of the total test time was also achieved in comparison with the current standard test.

Acknowledgements

Data availability

Supplementary data required to reproduce these findings are available in Appendix A, Appendix B, and Appendix C.

References

[1] C. Bak, F. Zahle, R. Bitsche, T. Kim, A. Yde, L. C. Henriksen, M. H. Hansen, J. A. A. Blasques, M. Gaunaa, A. Natarajan, The dtu 10-mw reference wind turbine, Tech. rep., Technical University of Denmark, DTU Wind Energy, Denmark (2013).

28

[2] O. Castro, P. Berring, K. Branner, C. F. Hvejsel, S. C. Yeniceli, F. Belloni, Bending-moment-based approach to match damage-equivalent strains in fatigue testing, Eng Struct (submitted for publication) (2020) xx–xx.

[3] IEC, Wind turbines – part 23: Full-scale structural testing of rotor blades, Standard, International Electrotechnical Commission (IEC) (April 2014).

[4] DNV-GL, Rotor blades for wind turbines, Standard, DNV-GL (Dec 2015).

[5] M. Quaresimin, L. Susmel, R. Talreja, Fatigue behaviour and life assessment of composite laminates under multiaxial loadings, Int J Fatigue 32 (1) (2010) 2–16. doi:10.1016/j.ijfatigue.2009.02.012.

[6] D. Zarouchas, R. Nijssen, Mechanical behaviour of thick structural adhesives in wind turbine blades under multi-axial loading, J Adhes Sci Technol 30 (13) (2016) 1413–1429. doi:10.1080/01694243.2016.1146392.

[7] J. Yoders, Are four wind-turbine failures in five weeks too many for nextera energy?
URL https://www.enr.com/articles/42352-are-four-wind-turbine-failures-in-five-weeks-too

[8] S. D. Hughes, W. D. Musial, T. Stensland, Implementation of a two-axis servo-hydraulic system for full-scale fatigue testing of wind turbine blades, Technical Report NREL/CP-500-26896, National Renewable Energy Laboratory, Golden (CO) (Aug 1999).

[9] D. L. White, A new method for dual-axis fatigue testing of large wind turbine blades using resonance excitation and spectral loading, Technical Report NREL/TP-500-35268, National Renewable Energy Laboratory, Golden (CO) (Apr 2004).

[10] J. A. Beckwith, Proof of concept test for dual-axis resonant phase-locked excitation (phlex) fatigue testing method for wind turbine blades, Ph.D. thesis, Embry-Riddle Aeronautical University (2014).

29

[11] N. Post, Fatigue test design: Scenarios for biaxial fatigue testing of a 60-meter wind turbine blade, Technical Report NREL/TP-5000-65227, National Renewable Energy Laboratory, Golden (CO) (Jul 2016).

[12] M. Desmond Jr., D. White, W. Barott, Finite element modeling of a dual axis resonant test system for wind turbine blades, in: Proceedings of the Asme 3rd International Conference on Energy Sustainability 2009, Es2009, Vol. 2, American Society of Mechanical Engineers, 2009, pp. 951–960. `doi:10.1115/ES2009-90164`.

[13] P. R. Greaves, R. G. Dominy, G. L. Ingram, H. Long, R. Court, Evaluation of dual-axis fatigue testing of large wind turbine blades, J Mech Eng Sci 226 (7) (2011) 1693–1704. `doi:10.1177/0954406211428013`.
URL `http://pic.sagepub.com/lookup/doi/10.1177/0954406211428013`

[14] F. Bürkner, A. Van Wingerde, Testing of rotor blades, in: Proceedings of the 8th International Conference on Structural Dynamics, Eurodyn 2011, European Assoc Structural Dynamics, 2011, pp. 3511–3517.

[15] D. Snowberg, S. Dana, S. Hughes, Implementation of a biaxial resonant fatigue test method on a large wind turbine blade, Technical Report NREL/TP-5000-61127, National Renewable Energy Laboratory, Golden (CO) (Sept 2014).

[16] P. Greaves, Fatigue analysis and testing of wind turbine blades, Ph.D. thesis, Durham University, Durham (Eng) (May 2013).

[17] P. Greaves, R. Prieto, P. Mckeever, R. Dominy, G. Ingram, Bi-axial fatigue testing of wind turbine blades, in: Proceedings of the European Wind Energy Association Conference, 2015.

[18] D. White, M. Desmond, W. Gowharji, J. A. Beckwith, K. J. Meierjurgen II, Development of a dual-axis phase locked resonant excitation test method for fatigue testing of wind turbine blades, in: Proceedings of the Asme

2011 International Mechanical Engineering Congress and Exposition, Imece 2011, Vol. 4, American Society of Mechanical Engineers, 2011, pp. 1163–1172.

[19] H. G. Lee, J. S. Park, Optimization of resonance-type fatigue testing for a full-scale wind turbine blade, Wind Energy 19 (2) (2016) 371–380. `doi: 10.1002/we.1837`.

[20] D. Melcher, M. Bätge, S. Neßlinger, A novel rotor blade fatigue test setup with elliptical biaxial resonant excitation, Wind Energy Sci Discuss 2019 (2019) 1–17. `doi:10.5194/wes-2019-84`.
URL `https://www.wind-energ-sci-discuss.net/wes-2019-84/`

[21] S. Timoshenko, History of strength of materials: With a brief account of the history of theory of elasticity and theory of structures, Dover Civil and Mechanical Engineering Series, Dover Publications, 1983.
URL `https://books.google.dk/books?id=tkScQmyhsb8C`

[22] J. P. A. A. Blasques, M. Stolpe, Multi-material topology optimization of laminated composite beam cross sections, Compos Struct 94 (11) (2012) 3278–3289.

[23] W. Yu, D. H. Hodges, V. Volovoi, C. E. S. Cesnik, On timoshenko-like modeling of initially curved and twisted composite beams, Int J Solids Struct 39 (19) (2002) 5101 – 5121. `doi:https://doi.org/10.1016/S0020-7683(02)00399-2`.
URL `http://www.sciencedirect.com/science/article/pii/S0020768302003992`

[24] D. V. Hutton, Fundamentals of finite element analysis, McGraw-Hill series in mechanical engineering, McGraw-Hill, 2004.
URL `https://books.google.dk/books?id=rQSiQgAACAAJ`

[25] A. Palmgren, Die lebensdauer von kugellagern, Z Ver Dtsch Ing 68 (14) (1924) 339–341.

[26] M. A. Miner, Cumulative damage in fatigue, J Appl Mech-T Asme 12 (3)
        (1945) A159–A164.

[27] M. Kawai, K. Yang, S. Oh, Effect of alternating r-ratios loading on fatigue
        life of woven fabric carbon/epoxy laminates, J Compos Mat 49 (27) (2015)
        3387–3405. `doi:10.1177/0021998314562847`.

[28] T. Kim, A. M. Hansen, K. Branner, Development of an anisotropic
        beam finite element for composite wind turbine blades in multi-
        body system, Renewable Energy 59 (2013) 172 – 183. `doi:https://doi.org/10.1016/j.renene.2013.03.033`.
        URL `http://www.sciencedirect.com/science/article/pii/S0960148113001894`

[29] S. S. Rao, Vibration of Continuous Systems, John Wiley and Sons, 2007.
        `doi:10.1002/9780470117866`.

[30] C. Galinos, T. J. Larsen, Aeroelastic analysis of b49 blade-blatigue project,
        Technical Report DTU Wind Energy I, Vol. 638, DTU Wind Energy (2018).

[31] D. G. Luenberger, Y. Ye, Linear and nonlinear programming, Springer
        International Publishing, 2016.

[32] S. J. Wright, Primal-dual interior-point methods, SIAM, 1997.

[33] Olsen Wings A/S.
        URL `http://olsenwings.dk/`

[34] H. G. Lee, J. Lee, Damping mechanism model for fatigue testing of a
        full-scale composite wind turbine blade, part 1: Modeling, Compos Struct
        202 (2018) 1216 – 1228.
        URL `http://www.sciencedirect.com/science/article/pii/S0263822318304367`

[35] C. Grinderslev, F. Belloni, S. G. Horcas, N. N. Sørensen, Investigations of
        aerodynamic drag forces during structural blade testing using high-fidelity

fluid–structure interaction, Wind Energy Sci 5 (2) (2020) 543–560. `doi:`
`10.5194/wes-5-543-2020`.
URL `https://wes.copernicus.org/articles/5/543/2020/`

[36] R. Crandall, C. Pomerance, Prime Numbers: A Computational Perspective, Springer New York, 2001.

[37] X. Chen, Experimental investigation on structural collapse of a large composite wind turbine blade under combined bending and torsion, Compos Struct 160 (2017) 435 – 445.
URL `http://www.sciencedirect.com/science/article/pii/`
`S0263822316312272`

[38] Germanischer Lloyd, Rules and Guidelines Industrial Services: Guideline for the Certification of Offshore Wind Turbines (2005) 155 – 164(pdf).
URL `http://www.gl-group.com/pdf/2012-12{_}GL{_}RC{_}Offshore{_}Guideline.`
`pdf`

Appendix A. Structural blade properties

Table A.6: Radial position, r; mass per unit length, m_g; radius of inertia with respect to elastic center, ri_x and ri_y; flapwise bending stiffness, EI_x; edgewise bending stiffness, EI_y; torsional stiffness, GJ; axial stiffness, EA; structural pitch, θ_p.

r	m_g	ri_x	ri_y	EI_x	EI_y	GJ	EA	θ_p
[m]	[kg/m]	[m]	[m]	[N.m^2]	[N.m^2]	[N.m^2/rad]	[N]	[°]
0.00	2.71E+02	2.31E-01	2.32E-01	3.20E+08	2.17E+08	6.69E+07	4.82E+09	1.60E+01
0.75	1.80E+02	2.41E-01	2.90E-01	1.89E+08	1.66E+08	5.34E+07	1.45E+09	-1.25E+01
1.50	1.09E+02	2.33E-01	3.11E-01	5.88E+07	1.15E+08	3.05E+07	8.68E+08	-1.20E+01
2.18	7.37E+01	2.06E-01	3.02E-01	4.17E+07	9.00E+07	2.09E+07	7.69E+08	-9.09E+00
2.75	6.63E+01	1.75E-01	2.89E-01	2.99E+07	9.60E+07	1.51E+07	7.55E+08	-6.62E+00
3.50	6.17E+01	1.36E-01	2.65E-01	1.75E+07	7.54E+07	8.67E+06	7.64E+08	-5.47E+00
4.00	5.74E+01	1.14E-01	2.44E-01	1.32E+07	5.25E+07	5.96E+06	7.56E+08	-4.64E+00
4.50	5.41E+01	9.77E-02	2.24E-01	9.76E+06	3.67E+07	4.14E+06	7.28E+08	-3.75E+00
5.50	4.78E+01	7.46E-02	1.98E-01	4.70E+06	2.29E+07	2.16E+06	5.99E+08	-1.40E+00
6.10	4.34E+01	6.52E-02	1.83E-01	3.17E+06	1.81E+07	1.55E+06	5.31E+08	-1.29E+00
7.00	3.72E+01	5.49E-02	1.65E-01	2.12E+06	1.24E+07	1.00E+06	4.42E+08	-8.57E-01
8.25	3.02E+01	4.57E-02	1.45E-01	1.10E+06	7.86E+06	6.10E+05	3.44E+08	-7.10E-01
9.00	2.66E+01	4.20E-02	1.38E-01	7.30E+05	6.03E+06	4.64E+05	2.74E+08	-4.82E-01
9.75	2.31E+01	3.89E-02	1.33E-01	5.39E+05	5.08E+06	3.71E+05	2.31E+08	-6.07E-01
11.00	1.92E+01	3.40E-02	1.28E-01	3.40E+05	3.28E+06	2.79E+05	1.75E+08	-5.74E-01
12.00	1.58E+01	2.91E-02	1.21E-01	2.01E+05	2.49E+06	1.76E+05	1.38E+08	-3.08E-01
13.55	7.08E+00	1.46E-02	7.84E-02	5.38E+04	9.35E+05	3.15E+04	6.60E+07	-7.62E-01
14.30	1.31E+00	1.42E-03	1.03E-02	5.00E+02	5.00E+02	4.60E+01	4.51E+06	-1.98E+00

34

Table A.7: Radial position, r; chord length, c; ratio between profile chord and height, c/t.

r	c	c/t	r	c	c/t
[m]	[m]	[−]	[m]	[m]	[−]
0.00	7.21E-01	1.00E+02	9.37	5.77E-01	2.04E+01
0.50	6.94E-01	1.00E+02	9.94	5.56E-01	2.01E+01
1.03	1.13E+00	5.72E+01	10.50	5.40E-01	1.96E+01
1.59	1.32E+00	4.40E+01	11.00	5.26E-01	1.91E+01
2.18	1.33E+00	3.89E+01	11.40	5.11E-01	1.86E+01
2.80	1.28E+00	3.43E+01	11.90	4.93E-01	1.80E+01
3.45	1.20E+00	2.98E+01	12.30	4.70E-01	1.74E+01
4.11	1.10E+00	2.64E+01	12.60	4.41E-01	1.68E+01
4.79	1.01E+00	2.40E+01	12.90	4.06E-01	1.62E+01
5.47	9.10E-01	2.27E+01	13.20	3.63E-01	1.57E+01
6.16	8.24E-01	2.19E+01	13.50	3.13E-01	1.52E+01
6.83	7.50E-01	2.15E+01	13.70	2.55E-01	1.47E+01
7.50	6.89E-01	2.12E+01	14.00	1.90E-01	1.44E+01
8.15	6.41E-01	2.10E+01	14.10	1.18E-01	1.40E+01
8.77	6.04E-01	2.07E+01	14.30	3.96E-02	1.37E+01

Table A.8: Section number, sec; half-chord coordinates, x_{pos}, y_{pos}, and z_{pos}; aerodynamic twist, β.

sec	x_{pos}	y_{pos}	z_{pos}	β	sec	x_{pos}	y_{pos}	z_{pos}	β
[−]	[m]	[m]	[m]	[°]	[−]	[m]	[m]	[m]	[°]
1	0.00E+00	0.00E+00	0.00E+00	-1.60E+01	11	-1.03E-01	4.36E-03	7.52E+00	-2.43E+00
2	-4.78E-02	1.38E-02	7.46E-01	-1.60E+01	12	-9.48E-02	3.11E-03	8.27E+00	-1.88E+00
3	-1.87E-01	5.16E-02	1.49E+00	-1.54E+01	13	-8.87E-02	2.35E-03	9.02E+00	-1.52E+00
4	-1.94E-01	4.84E-02	2.24E+00	-1.40E+01	14	-8.42E-02	1.91E-03	9.78E+00	-1.30E+00
5	-1.85E-01	3.94E-02	2.99E+00	-1.20E+01	15	-8.08E-02	1.63E-03	1.05E+01	-1.16E+00
6	-1.71E-01	2.96E-02	3.75E+00	-9.82E+00	16	-7.74E-02	1.39E-03	1.13E+01	-1.03E+00
7	-1.56E-01	2.10E-02	4.50E+00	-7.68E+00	17	-7.25E-02	1.05E-03	1.20E+01	-8.27E-01
8	-1.40E-01	1.43E-02	5.25E+00	-5.83E+00	18	-6.33E-02	4.65E-04	1.28E+01	-4.21E-01
9	-1.26E-01	9.56E-03	6.01E+00	-4.35E+00	19	-4.51E-02	-3.09E-04	1.35E+01	3.92E-01
10	-1.13E-01	6.40E-03	6.76E+00	-3.23E+00	20	-5.94E-03	-2.07E-04	1.43E+01	2.00E+00

35

Appendix B. Equivalent target strain amplitude

Table B.9: Equivalent target strain amplitude, $\hat{\varepsilon}^{tgt}_{amp,i}$, along the blade in $[m/m]$ for $\hat{m} = 10$ and $\hat{n} = 2E6$ cycles.

Cross-section point	r [m]																	
	0.00	0.75	1.50	2.18	2.75	3.00	3.50	4.00	4.50	5.50	6.10	7.00	8.25	9.00	9.75	10.00	11.00	12.00
1	1.52E-04	2.26E-04	4.76E-04	5.23E-04	4.34E-04	4.26E-04	4.47E-04	5.25E-04	6.22E-04	7.26E-04	7.51E-04	7.68E-04	6.86E-04	5.88E-04	5.17E-04	5.05E-04	3.91E-04	2.49E-04
2	21.47E-04	2.06E-04	4.72E-04	4.99E-04	4.08E-04	4.00E-04	4.22E-04	5.04E-04	6.02E-04	7.15E-04	7.44E-04	7.60E-04	6.69E-04	5.44E-04	4.56E-04	4.39E-04	3.42E-04	2.14E-04
3	1.42E-04	1.95E-04	4.65E-04	4.43E-04	3.52E-04	3.42E-04	3.69E-04	4.66E-04	5.61E-04	7.03E-04	7.44E-04	7.60E-04	6.71E-04	5.12E-04	3.92E-04	3.54E-04	2.77E-04	1.63E-04
4	1.39E-04	1.90E-04	4.30E-04	4.14E-04	3.29E-04	3.21E-04	3.57E-04	4.54E-04	5.45E-04	7.12E-04	7.68E-04	7.81E-04	7.03E-04	5.27E-04	3.95E-04	3.40E-04	2.58E-04	1.33E-04
5	1.38E-04	1.86E-04	3.69E-04	3.97E-04	3.22E-04	3.20E-04	3.64E-04	4.59E-04	5.42E-04	7.39E-04	8.15E-04	8.23E-04	7.65E-04	5.81E-04	4.51E-04	3.92E-04	2.92E-04	1.51E-04
6	1.40E-04	1.84E-04	3.27E-04	3.94E-04	3.31E-04	3.36E-04	3.91E-04	4.80E-04	5.54E-04	7.84E-04	8.85E-04	8.90E-04	8.60E-04	6.70E-04	5.47E-04	4.88E-04	3.58E-04	2.00E-04
7	1.44E-04	1.84E-04	3.06E-04	4.05E-04	3.56E-04	3.69E-04	4.35E-04	5.16E-04	5.84E-04	8.48E-04	9.73E-04	9.78E-04	9.84E-04	7.89E-04	6.70E-04	6.14E-04	4.49E-04	2.67E-04
8	1.49E-04	1.90E-04	3.02E-04	4.30E-04	3.95E-04	4.16E-04	4.93E-04	5.67E-04	6.28E-04	9.24E-04	1.08E-03	1.08E-03	1.13E-03	9.25E-04	8.11E-04	7.56E-04	5.52E-04	3.43E-04
9	1.54E-04	1.97E-04	3.18E-04	4.57E-04	4.44E-04	4.70E-04	5.49E-04	6.12E-04	6.70E-04	1.00E-03	1.19E-03	1.20E-03	1.28E-03	1.04E-03	9.32E-04	8.72E-04	6.40E-04	4.24E-04
10	1.60E-04	2.08E-04	3.43E-04	5.00E-04	5.00E-04	5.31E-04	6.18E-04	6.76E-04	7.33E-04	1.10E-03	1.30E-03	1.32E-03	1.44E-03	1.19E-03	1.08E-03	1.03E-03	7.56E-04	5.05E-04
11	1.65E-04	2.18E-04	3.89E-04	5.49E-04	5.58E-04	5.94E-04	6.88E-04	7.45E-04	8.01E-04	1.19E-03	1.42E-03	1.44E-03	1.60E-03	1.34E-03	1.23E-03	1.18E-03	8.69E-04	5.82E-04
12	1.69E-04	2.30E-04	4.43E-04	6.01E-04	6.18E-04	6.57E-04	7.59E-04	8.15E-04	8.71E-04	1.28E-03	1.54E-03	1.56E-03	1.76E-03	1.49E-03	1.38E-03	1.33E-03	9.77E-04	6.55E-04
13	1.73E-04	2.43E-04	5.02E-04	6.53E-04	6.76E-04	7.21E-04	8.30E-04	8.83E-04	9.42E-04	1.37E-03	1.65E-03	1.67E-03	1.90E-03	1.62E-03	1.52E-03	1.46E-03	1.07E-03	7.20E-04
14	1.76E-04	2.55E-04	5.59E-04	7.04E-04	7.32E-04	7.82E-04	8.99E-04	9.49E-04	1.01E-03	1.45E-03	1.75E-03	1.77E-03	2.03E-03	1.75E-03	1.64E-03	1.58E-03	1.16E-03	7.75E-04
15	1.78E-04	2.67E-04	6.13E-04	7.52E-04	7.84E-04	8.38E-04	9.63E-04	1.01E-03	1.07E-03	1.53E-03	1.83E-03	1.86E-03	2.14E-03	1.85E-03	1.74E-03	1.67E-03	1.23E-03	8.18E-04
16	1.79E-04	2.76E-04	6.60E-04	7.86E-04	8.22E-04	8.80E-04	1.01E-03	1.06E-03	1.11E-03	1.58E-03	1.89E-03	1.92E-03	2.22E-03	1.92E-03	1.81E-03	1.74E-03	1.27E-03	8.46E-04
17	1.79E-04	2.81E-04	6.92E-04	8.25E-04	8.65E-04	9.25E-04	1.06E-03	1.10E-03	1.14E-03	1.60E-03	1.92E-03	1.94E-03	2.25E-03	1.95E-03	1.84E-03	1.77E-03	1.29E-03	8.57E-04
18	1.78E-04	2.84E-04	7.24E-04	8.58E-04	9.00E-04	9.62E-04	1.10E-03	1.13E-03	1.16E-03	1.62E-03	1.93E-03	1.95E-03	2.26E-03	1.95E-03	1.85E-03	1.77E-03	1.29E-03	8.49E-04
19	1.77E-04	2.83E-04	7.45E-04	8.80E-04	9.23E-04	9.83E-04	1.11E-03	1.14E-03	1.18E-03	1.60E-03	1.90E-03	1.91E-03	2.21E-03	1.91E-03	1.81E-03	1.72E-03	1.25E-03	8.18E-04
20	1.74E-04	2.79E-04	7.54E-04	8.88E-04	9.29E-04	9.87E-04	1.11E-03	1.13E-03	1.18E-03	1.56E-03	1.83E-03	1.82E-03	2.11E-03	1.81E-03	1.73E-03	1.63E-03	1.18E-03	7.64E-04
21	1.72E-04	2.71E-04	7.49E-04	8.82E-04	9.16E-04	9.69E-04	1.09E-03	1.10E-03	1.12E-03	1.46E-03	1.71E-03	1.69E-03	1.94E-03	1.66E-03	1.59E-03	1.49E-03	1.08E-03	6.87E-04
22	1.69E-04	2.63E-04	7.31E-04	8.56E-04	8.77E-04	9.24E-04	1.04E-03	1.05E-03	1.07E-03	1.33E-03	1.54E-03	1.51E-03	1.72E-03	1.52E-03	1.45E-03	1.35E-03	9.61E-04	5.87E-04
23	1.65E-04	2.49E-04	6.92E-04	8.05E-04	8.10E-04	8.48E-04	9.46E-04	9.59E-04	9.77E-04	1.16E-03	1.32E-03	1.26E-03	1.43E-03	1.27E-03	1.22E-03	1.11E-03	7.81E-04	4.54E-04
24	1.61E-04	2.39E-04	6.55E-04	7.58E-04	7.49E-04	7.78E-04	8.62E-04	8.76E-04	8.97E-04	1.02E-03	1.13E-03	1.06E-03	1.19E-03	1.06E-03	1.03E-03	9.13E-04	6.32E-04	3.47E-04
25	1.56E-04	2.16E-04	5.51E-04	6.26E-04	5.77E-04	5.85E-04	6.39E-04	6.45E-04	6.48E-04	6.31E-04	6.44E-04	5.81E-04	5.90E-04	5.50E-04	5.26E-04	4.89E-04	3.26E-04	1.36E-04
26	1.51E-04	1.97E-04	4.81E-04	5.37E-04	4.62E-04	4.55E-04	4.76E-04	4.71E-04	4.63E-04	4.09E-04	4.15E-04	4.40E-04	4.21E-04	3.96E-04	2.70E-04	3.09E-04	2.52E-04	2.11E-04
27	1.46E-04	1.83E-04	4.00E-04	4.35E-04	3.39E-04	3.16E-04	3.06E-04	3.12E-04	3.50E-04	4.93E-04	6.02E-04	7.24E-04	9.21E-04	7.87E-04	5.85E-04	6.57E-04	5.26E-04	4.26E-04
28	1.42E-04	1.71E-04	3.32E-04	3.46E-04	2.81E-04	2.73E-04	2.69E-04	3.17E-04	4.06E-04	7.18E-04	8.90E-04	9.80E-04	1.29E-03	1.10E-03	9.32E-04	9.50E-04	7.39E-04	5.59E-04
29	1.39E-04	1.63E-04	3.33E-04	3.42E-04	3.37E-04	3.55E-04	3.75E-04	4.18E-04	5.08E-04	8.92E-04	1.12E-03	1.23E-03	1.57E-03	1.34E-03	1.18E-03	1.17E-03	9.00E-04	6.58E-04
30	1.38E-04	1.64E-04	3.69E-04	3.76E-04	4.23E-04	4.62E-04	5.01E-04	5.32E-04	6.15E-04	1.05E-03	1.32E-03	1.43E-03	1.80E-03	1.54E-03	1.39E-03	1.35E-03	1.03E-03	7.28E-04
31	1.41E-04	1.71E-04	4.07E-04	4.11E-04	5.03E-04	5.56E-04	5.95E-04	6.08E-04	6.93E-04	1.17E-03	1.47E-03	1.59E-03	1.97E-03	1.65E-03	1.53E-03	1.46E-03	1.11E-03	7.78E-04
32	1.45E-04	1.81E-04	4.59E-04	4.53E-04	5.69E-04	6.27E-04	6.79E-04	6.91E-04	7.69E-04	1.26E-03	1.58E-03	1.68E-03	2.09E-03	1.76E-03	1.64E-03	1.57E-03	1.18E-03	8.15E-04
33	1.50E-04	1.88E-04	5.02E-04	4.88E-04	6.14E-04	6.76E-04	7.37E-04	7.45E-04	8.16E-04	1.31E-03	1.64E-03	1.73E-03	2.15E-03	1.82E-03	1.71E-03	1.63E-03	1.22E-03	8.35E-04
34	1.56E-04	2.02E-04	5.42E-04	5.22E-04	6.50E-04	7.14E-04	7.82E-04	7.86E-04	8.47E-04	1.33E-03	1.66E-03	1.74E-03	2.16E-03	1.85E-03	1.76E-03	1.66E-03	1.24E-03	8.41E-04
35	1.62E-04	2.14E-04	5.61E-04	5.42E-04	6.65E-04	7.29E-04	8.01E-04	7.99E-04	8.49E-04	1.31E-03	1.63E-03	1.71E-03	2.13E-03	1.83E-03	1.76E-03	1.65E-03	1.23E-03	8.35E-04
36	1.67E-04	2.27E-04	5.72E-04	5.49E-04	6.66E-04	7.28E-04	8.01E-04	7.94E-04	8.35E-04	1.28E-03	1.59E-03	1.66E-03	2.07E-03	1.78E-03	1.72E-03	1.61E-03	1.21E-03	8.14E-04
37	1.72E-04	2.38E-04	5.70E-04	5.50E-04	6.55E-04	7.12E-04	7.79E-04	7.71E-04	8.11E-04	1.21E-03	1.50E-03	1.56E-03	1.94E-03	1.68E-03	1.63E-03	1.53E-03	1.15E-03	7.79E-04
38	1.76E-04	2.45E-04	5.56E-04	5.39E-04	6.31E-04	6.84E-04	7.41E-04	7.31E-04	7.67E-04	1.11E-03	1.37E-03	1.42E-03	1.78E-03	1.54E-03	1.51E-03	1.42E-03	1.06E-03	7.32E-04
39	1.79E-04	2.51E-04	5.33E-04	5.19E-04	5.97E-04	6.43E-04	6.89E-04	6.76E-04	7.08E-04	9.89E-04	1.21E-03	1.26E-03	1.58E-03	1.38E-03	1.36E-03	1.28E-03	9.64E-04	6.73E-04
40	1.81E-04	2.54E-04	5.04E-04	4.92E-04	5.54E-04	5.93E-04	6.28E-04	6.10E-04	6.37E-04	8.56E-04	1.04E-03	1.08E-03	1.36E-03	1.19E-03	1.20E-03	1.13E-03	8.53E-04	6.04E-04
41	1.82E-04	2.53E-04	4.72E-04	4.60E-04	5.04E-04	5.36E-04	5.59E-04	5.39E-04	5.63E-04	7.20E-04	8.66E-04	8.94E-04	1.13E-03	1.00E-03	1.03E-03	9.75E-04	7.39E-04	5.34E-04
42	1.82E-04	2.49E-04	4.43E-04	4.27E-04	4.52E-04	4.77E-04	4.89E-04	4.71E-04	4.97E-04	5.94E-04	6.96E-04	7.12E-04	9.06E-04	8.18E-04	8.54E-04	8.20E-04	6.27E-04	4.64E-04
43	1.81E-04	2.43E-04	4.20E-04	3.98E-04	4.03E-04	4.20E-04	4.25E-04	4.15E-04	4.44E-04	4.90E-04	5.52E-04	5.61E-04	7.13E-04	6.93E-04	6.96E-04	7.03E-04	5.41E-04	3.99E-04
44	1.79E-04	2.36E-04	4.00E-04	3.80E-04	3.61E-04	3.74E-04	3.83E-04	3.81E-04	4.10E-04	4.31E-04	4.62E-04	4.69E-04	5.68E-04	5.61E-04	5.94E-04	5.82E-04	4.51E-04	3.40E-04
45	1.76E-04	2.26E-04	3.91E-04	3.66E-04	3.31E-04	3.38E-04	3.46E-04	3.58E-04	3.99E-04	4.31E-04	4.50E-04	4.65E-04	4.83E-04	4.71E-04	4.66E-04	4.83E-04	3.80E-04	2.90E-04
46	1.73E-04	2.15E-04	3.96E-04	3.65E-04	3.17E-04	3.19E-04	3.30E-04	3.61E-04	4.19E-04	4.84E-04	5.04E-04	5.23E-04	4.73E-04	4.29E-04	4.06E-04	4.18E-04	3.32E-04	2.53E-04
47	1.70E-04	2.05E-04	4.18E-04	3.79E-04	3.21E-04	3.19E-04	3.35E-04	3.86E-04	4.58E-04	5.46E-04	5.74E-04	5.95E-04	5.19E-04	4.32E-04	3.84E-04	3.88E-04	3.10E-04	2.29E-04
48	1.66E-04	1.95E-04	4.61E-04	4.08E-04	3.40E-04	3.36E-04	3.57E-04	4.21E-04	5.01E-04	6.02E-04	6.35E-04	6.60E-04	5.75E-04	4.64E-04	3.93E-04	3.90E-04	3.10E-04	2.21E-04
49	1.62E-04	2.00E-04	4.87E-04	4.47E-04	3.72E-04	3.64E-04	3.88E-04	4.59E-04	5.45E-04	6.47E-04	6.81E-04	7.08E-04	6.19E-04	5.04E-04	4.26E-04	4.19E-04	3.31E-04	2.27E-04
50	1.57E-04	2.09E-04	4.92E-04	4.95E-04	4.16E-04	4.13E-04	4.39E-04	5.06E-04	5.93E-04	6.83E-04	7.14E-04	7.40E-04	6.54E-04	5.53E-04	4.84E-04	4.78E-04	3.73E-04	2.48E-04

Appendix C. Ultimate and target fatigue bending moments

Table C.10: Maximum and minimum ultimate bending moments, U^{max} and U^{min} respectively, in flapwise and edgewise directions including safety factors; and target fatigue bending moments, M^{tgt}, in flapwise and edgewise directions for $\hat{m} = 10$ and $\hat{n} = 2E6$ cycles.

r	U_{flap}^{max}	U_{flap}^{min}	U_{edge}^{max}	U_{edge}^{min}	M_{flap}^{tgt}	M_{edge}^{tgt}
$[m]$	$[kNm]$	$[kNm]$	$[kNm]$	$[kNm]$	$[kNm]$	$[kNm]$
0.00	217.20	-285.50	86.00	-74.62	208.52	121.58
1.49	175.42	-228.85	64.94	-57.31	167.98	91.03
2.99	137.39	-176.42	51.19	-43.76	133.83	66.95
6.01	72.14	-91.91	27.73	-24.82	75.80	32.02
6.76	58.35	-75.04	22.94	-21.32	62.47	25.71
9.02	27.20	-34.57	11.78	-11.62	30.89	11.54
12.04	4.16	-4.73	2.18	-2.12	4.60	1.59
13.55	0.30	-0.30	0.19	-0.19	0.34	0.12

Appendix D. Standard fatigue test

In this appendix, additional information regarding the standard test simulation is provided. The ratio between test fatigue bending moments, M^{test}, and the target bending moments, M^{tgt}, for the flapwise and edgewise standard tests is presented in Fig. D.11. In addition, a comparison between the maximum and minimum fatigue bending moments applied during the test, $M_{fatigue}$, and the static ultimate bending moments of the blade, $M_{ultimate}$, is shown in Fig. D.12. Finally, the equivalent damage ratio, EDR, along the blade after the single-axial edgewise and the single-axial flapwise standard tests is shown in Fig. D.13.
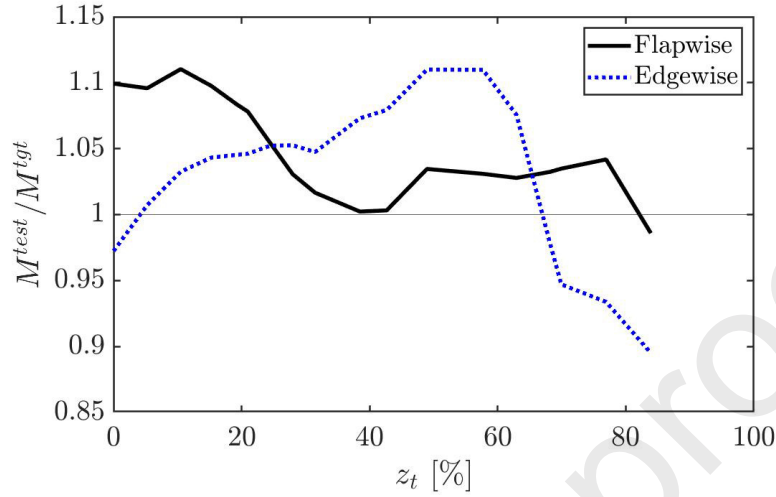
Figure D.11: Ratio between the test bending moments, M^{test}, and the target bending moments, M^{tgt}, for both standard flapwise test and standard edgewise test.
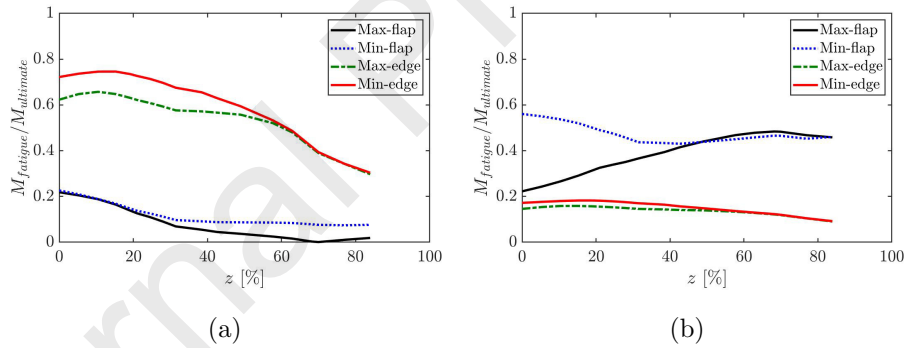

Figure D.12: Comparison between the maximum and minimum loads during the test, $M_{fatigue}$, in flapwise and edgewise directions respect to the static ultimate loads, $M_{ultimate}$, for (a) the standard edgewise fatigue test, and (b) the standard flapwise fatigue test.

Appendix E. All-combined-loading optimized fatigue test

Further information related to the all-combined-loading optimized solution is provided in this section. The comparison between the maximum and minimum
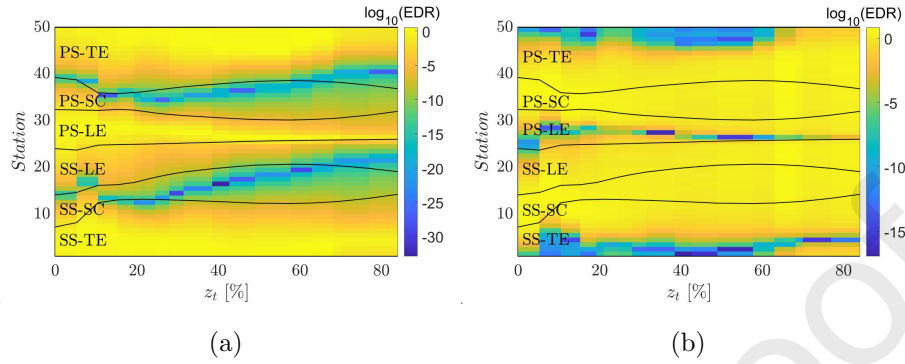
38

Figure D.13: EDR after (a) the standard edgewise fatigue test, and (b) the standard flapwise fatigue test. In log scale.

fatigue bending moments, $M_{fatigue}$, and the static ultimate bending moments, $M_{ultimate}$, for the different test configurations within the optimal solution is shown in Fig. E.14. Additionally, the equivalent damage ratio, EDR, along the blade after each of the different test configurations within the optimal solution

730   is shown in Fig. E.15.
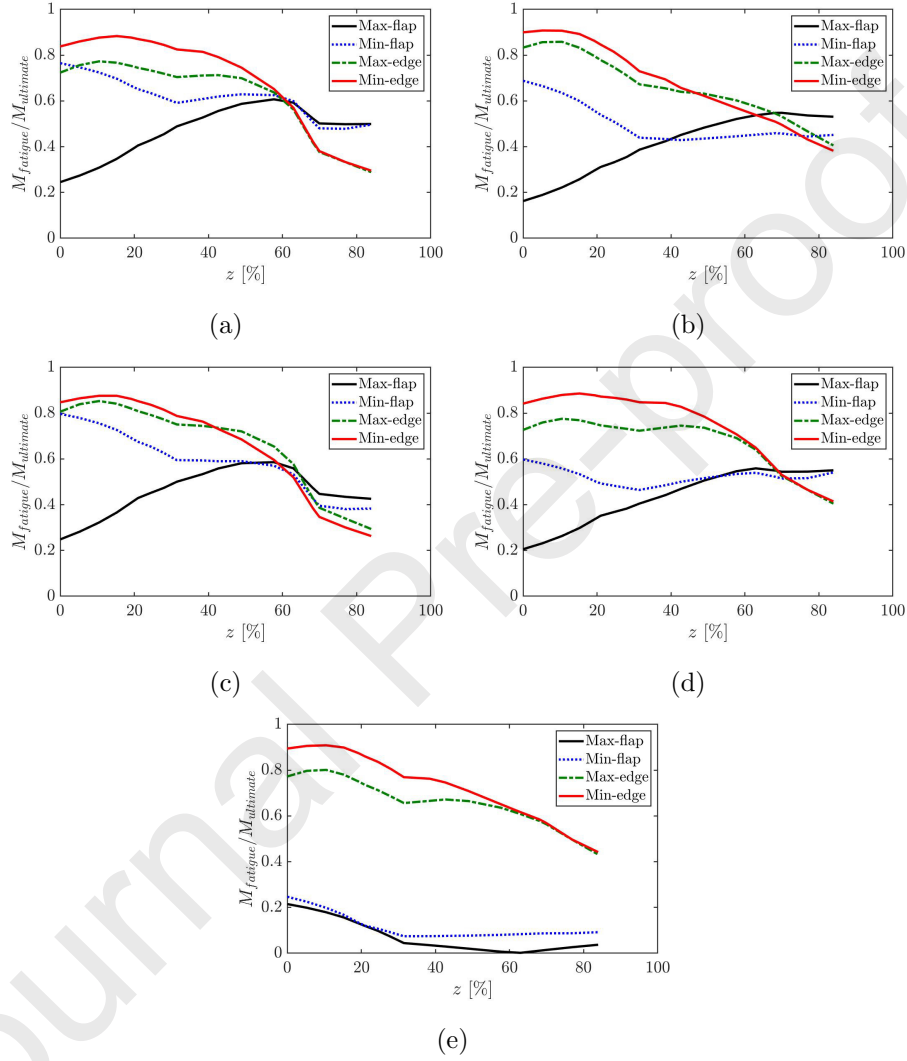
(a)

(b)

(c)

(d)

(e)

Figure E.14: Comparison between the maximum and minimum test loads in the flapwise and edgewise directions respect to the static ultimate loads for each type of test within the optimal solution (see Table 5): (a) Chaotic No 1; (b) Chaotic No 2; (c) Chaotic No 3; (d) Chaotic No 4; (e) Single-axial edgewise case.
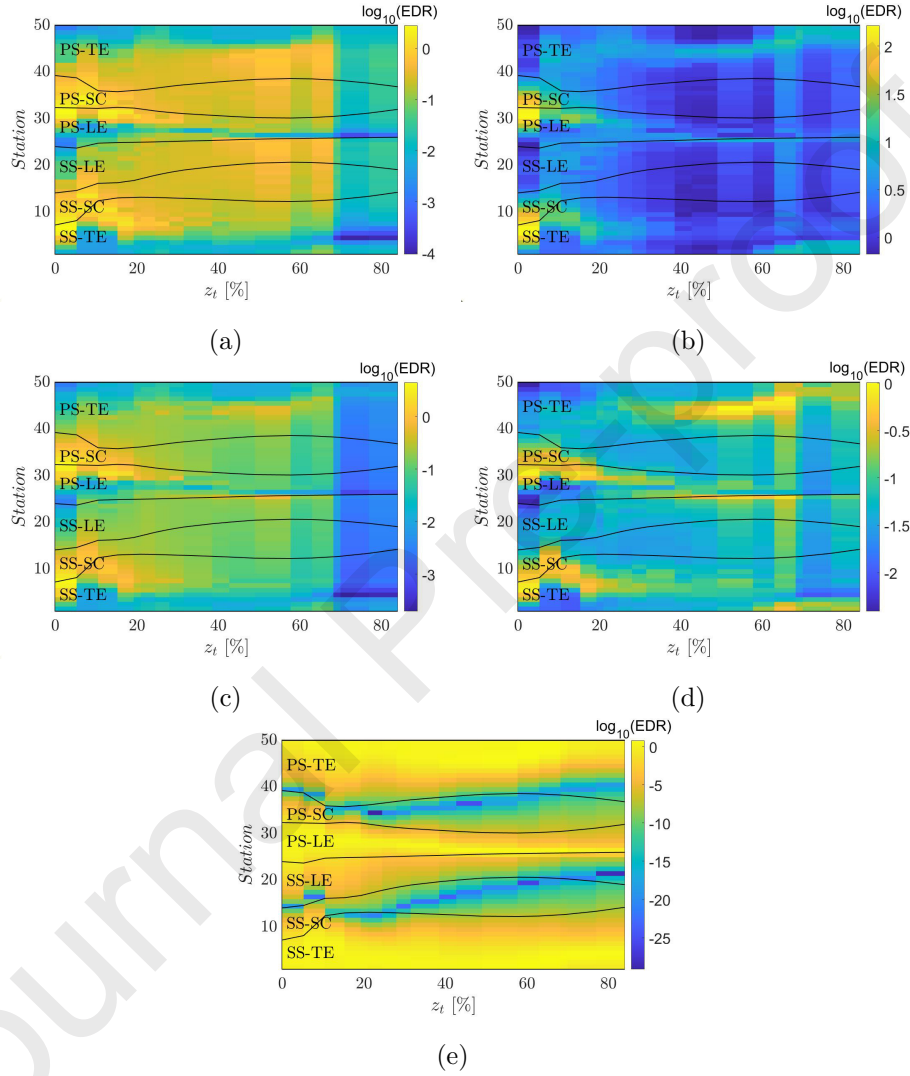
Figure E.15: *EDR* after each type of test within the optimal solution (see Table 5): (a) Chaotic No 1; (b) Chaotic No 2; (c) Chaotic No 3; (d) Chaotic No 4; (e) Single-axial edgewise case. In log scale.

41

Declaration of interests

☒ The authors declare that they have no known competing financial interests or personal relationships that could have appeared to influence the work reported in this paper.

☐The authors declare the following financial interests/personal relationships which may be considered as potential competing interests:

Oscar Castro: Conceptualization, Methodology, Software, Validation, Formal analysis, Investigation, Data Curation, Writing - Original Draft, Visualization, Supervision

Federico Belloni: Conceptualization, Methodology, Software, Validation, Formal analysis, Investigation, Resources, Writing - Review & Editing, Visualization

Mathias Stolpe: Conceptualization, Methodology, Software, Writing - Review & Editing

Süleyman Cem Yeniceli: Conceptualization, Methodology, Software, Validation, Formal analysis, Investigation, Resources, Data Curation, Writing - Review & Editing, Visualization

Peter Berring: Conceptualization, Methodology, Validation, Formal analysis, Investigation, Data Resources

Kim Branner: Conceptualization, Writing - Review & Editing, Supervision, Project administration, Funding acquisition